Effect of interface defect formation on carrier diffusion and luminescence in $In_{0.2}Ga_{0.8}As/Al_xGa_{1-x}As$ quantum wells

D. H. Rich,[a] K. Rammohan, H. T. Lin, and Y. Tang
Department of Materials Science and Engineering, University of Southern California, Los Angeles, California 90089-0241

M. Meshkinpour and M. S. Goorsky
Department of Materials Science and Engineering, University of California, Los Angeles, Los Angeles, California 90024

(Received 2 February 1996; accepted 17 April 1996)

We have examined the influence of strain relaxation on the excitonic recombination and diffusion in $In_{0.2}Ga_{0.8}As/Al_xGa_{1-x}As$ quantum-well (QW) samples designed for high-electron-mobility transistors, using spectrally and spatially resolved polarized cathodoluminescence (CL). Six molecular-beam epitaxial grown samples, with varying channel thicknesses ranging from 75 to 300 Å, were examined at various temperatures between 87 and 300 K. An increase in misfit dislocation density occurred with increasing channel thicknesses and resulted in changes in the dark line defect (DLD) density, polarization anisotropy, QW excitonic luminescence energy, and luminescence activation energy, as observed in CL. The influence of misfit dislocations on the ambipolar diffusion of excess carriers in a direction parallel to the dislocation line, in varying proximity to the DLDs, was examined with a CL-based diffusion experiment. The temperature dependence of the CL imaging was examined, enabling a study of the spatial variation of the activation energies associated with thermal quenching of the $GaAs/Al_{0.25}Ga_{0.75}As$ multiple QW and $In_{0.2}Ga_{0.8}As$ QW luminescence. The CL intensity exhibits an Arrenhius-type dependence on temperature and is controlled by thermally activated nonradiative recombination. The activation energies for both the $In_{0.2}Ga_{0.8}As$ QW and $Al_{0.25}Ga_{0.75}As$ MQW luminescence are found to vary spatially in close proximity to the misfit dislocations. We have utilized a new approach to obtain 2D images of the activation energies. The influence of the strain relaxation on the polarization and energy of the $In_{0.2}Ga_{0.8}As$ QW excitonic luminescence was examined with linearly polarized CL and CL wavelength imaging. A strain-induced modification of the luminescence energy and an increase in the polarization anisotropy was measured near DLDs. Thus, we find that certain DLDs exhibit significant polarization and energy variations in their optical properties, in addition to their more familiar nonradiative behavior. © *1996 American Vacuum Society.*

I. INTRODUCTION

The growth of high-quality strained films of $In_xGa_{1-x}As$ on GaAs substrates has several diverse applications in millimeter-wave electronic devices, such as high-electron-mobility transistors (HEMTs),[1–3] and near-infrared photonic devices, such as lasers[4–6] and light modulators.[7–10] The primary deleterious effect of strain relaxation is to introduce misfit dislocations at the $In_xGa_{1-x}As/GaAs$ interfaces which can serve as nonradiative recombination centers and impede the transport of carriers.[10–13] The generation of an asymmetrical density of 60° dislocations along the orthogonal $\langle 110 \rangle$ directions will also modify the biaxial symmetry of the strain tensor, and induce an asymmetry in the transport of carriers[10,12] and a polarization anisotropy in the excitonic luminescence.[14–16] Electron-beam probes which yield greater than a $\sim$1-μm-scale resolution, such as in spatially and spectrally resolved cathodoluminescence (CL), can help advance our understanding of the influence of defects on the optical and transport properties of quantum heterostructures. A dislocation-induced asymmetry in the ambipolar diffusion of excess carriers in nipi-doped $In_{0.2}Ga_{0.8}As/GaAs$ multiple quantum wells (MQWs) has been previously measured using an electron-beam-induced absorption modulation technique.[10,12] In other studies, changes in the polarization anisotropy and energy of excitonic luminescence in thick $In_xGa_{1-x}As/GaAs$ films were found to correlate with the position of dark line defects (DLDs) from studies of linearly polarized cathodoluminescence (LPCL) and CL wavelength imaging (CLWI).[14–16]

In this study we aim to further explore the interplay between the strain relaxation, optical properties, and transport properties in $In_{0.2}Ga_{0.8}As/Al_xGa_{1-x}As$ QW samples, designed for HEMTs, using LPCL and CLWI. A four-band $\mathbf{k}\cdot\mathbf{p}$ calculation is used to examine the energy and polarization variations caused by the strain relaxation. A self-consistent-field calculation using the transfer-matrix method is used to determine the electron and hole eigenstates in the channel and the excitonic transition energies.

The temperature dependence of luminescence in QWs and superlattices has been investigated previously;[17,18] however, only recently have we begun to examine the effects of ther-

[a]Electronic mail: danrich@alnitak.usc.edu

mal quenching of luminescence by misfit dislocations. Thermal quenching of the luminescence has been interpreted in several ways by different authors, and has been attributed to either thermal dissociation of excitons and thermally activated nonradiative recombination,[19] or due to thermal emission of carriers out of the QWs, resulting in a reduction of luminescence intensity at higher temperatures.[20] The temperature dependence of the CL imaging was examined here in the 87–250 K range, enabling a study of the spatial variation of the activation energies associated with thermal quenching of luminescence near individual dislocations. The CL intensity exhibits an Arrenhius-type dependence on the temperature and is controlled by thermally activated nonradiative recombination. We have utilized a new approach to obtain 2D images of the activation energy.

In particular, we have also examined the change in the ambipolar diffusion length of carriers parallel to and in close proximity to misfit dislocations using a CL-based diffusion experiment. The changes in diffusion length are measured in varying proximity to DLDs, and correlations with the CL intensity, activation energy, polarization anisotropy, and luminescence energy are established. A detailed study of the CLWI, LPCL, activation energy imaging, and ambipolar diffusion length variations is performed for two samples whose $In_{0.2}Ga_{0.8}As$ channel thicknesses are just beyond the critical thickness in order that fundamental optical and transport properties can be examined near individual dislocations with a ~ 1 μm spatial resolution. An examination of relaxation- and defect-induced changes in carrier diffusion and luminescence, on a μm scale, is further essential in enabling an evaluation of fundamental design and growth parameters necessary for optimized HEMT performance.

II. EXPERIMENT

Six HEMT devices were grown by molecular-beam epitaxy.[21–24] Each sample consisted of the following layers (in order from substrate to the surface) grown on semi-insulating GaAs(001) substrates: a 1750-Å-thick GaAs undoped buffer layer; a GaAs/$Al_{0.25}Ga_{0.75}As$ MQW (~42-Å-thick QWs); a 3000-Å-thick undoped GaAs barrier; an $In_{0.2}Ga_{0.8}As$ QW (channel) varying in thickness from 75 to 300 Å; a 530 Å layer of $Al_{0.25}Ga_{0.75}As$, containing a δ-doped Si layer ($\sim 5\times 10^{12}$ cm^{-2}) within about 30 Å of the channel; and a 50-Å-thick undoped GaAs cap. These samples were previously analyzed with transmission electron microscopy (TEM), triple-axis x-ray diffraction (XRD), and Hall measurements to establish a relationship between degradation of the device performance and the formation of $\langle 110\rangle$-oriented misfit dislocations.[21,22] That study established that the onset of a substantial device degradation occurred when misfit dislocations formed along both $\langle 110\rangle$ directions. High-resolution XRD further showed that the average In composition x in the samples varied from $0.203 \leqslant x \leqslant 0.214$.

Scanning monochromatic CL, panchromatic CL, CLWI, and LPCL were performed with a modified JEOL 840-A scanning electron microscope.[14–16] A rotatable linear polarizer was mounted *in vacuo* to perform polarization

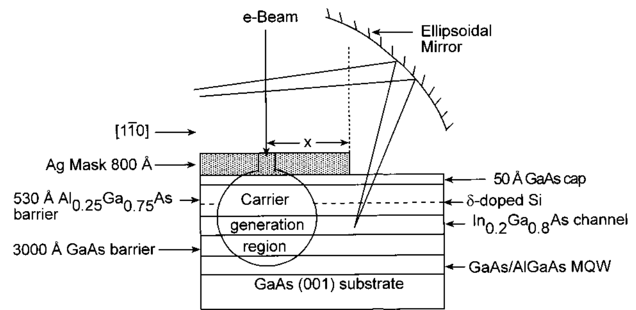

FIG. 1. Schematic diagram of the HEMT sample structure showing the ambipolar diffusion length experiment.

measurements.[25] The light collected was dispersed by a 0.25 m monochromator and detected with a liquid-nitrogen-cooled Ge p-i-n diode detector. CL spectra were obtained with a spectral resolution of 1 nm. An electron-beam energy of 12 keV with varying beam currents from 0.1 to 10 nA was used to probe the samples. The temperature of the samples was varied between 87 and 300 K, for the various CL measurements.

In CLWI, the wavelength λ_m at which the intensity of luminescence is a maximum is mapped as a function of the spatial (x,y) position, and a gray scale or false color image representing these wavelengths is generated.[14–16,26] A scanning area of 128×94 μm^2 is discretized into 640×480 pixels. In order to determine $\lambda_m(x,y)$, a spectrum consisting of 20 wavelength points (obtained from 20 discrete monochromatic CL images) was obtained at each (x,y) position, thereby enabling a mapping of the $In_{0.2}Ga_{0.8}As$ channel interband transition energy. The wavelength ranges for the 150 and 185 Å $In_{0.2}Ga_{0.8}As$ samples was from 960 to 965 nm and 967 to 977 nm, respectively. Spectrally integrated CL images (panchromatic in the specified wavelength range) were likewise obtained by summing the 20 discrete monochromatic images at each (x,y) pixel position.

LPCL imaging and spectroscopy measurements were taken with the polarizer rotated to detect the excitonic luminescence with $\mathbf{E}\perp[110]$ or $\mathbf{E}\parallel[110]$, where $\mathbf{E}$ is the electric field of the detected light. In order to emphasize the polarization variations, the ratio of the LPCL images at each (x,y) position is represented as $\log[I_\perp(x,y)/I_\parallel(x,y)]$, where $I_\perp$ and $I_\parallel$ are the pixel intensities under $\mathbf{E}\perp[110]$ and $\mathbf{E}\parallel[110]$ detection orientations, normalized to a 256-level gray scale. The $\perp$ and $\parallel$ subscripts are defined with respect to the $[110]$ direction in this study.

The ambipolar diffusion lengths were measured using an approach illustrated in Fig. 1. The HEMT samples were coated with a 800-Å-thick Ag mask over part of the sample. The Ag film had lateral dimensions of 100×100 μm^2, and the edges of these squares were oriented along the $\langle 110\rangle$ directions. The e-beam energy of 12 keV was sufficiently large so that ~80% of the beam penetrated the Ag film and

generated electrons and holes in the region just below the mask.[27] The Ag mask prevented light from radiative recombination in the generation region just below the mask from being detected by the CL collection system; however, luminescence from carriers which diffused along the $[1\bar{1}0]$ direction (as shown in Fig. 1) and recombined just beyond the edge of the mask was detected. By simultaneously scanning the e beam toward the edge of the mask and recording the integrated intensity of excitonic luminescence coming from the $In_{0.2}Ga_{0.8}As$ channel as a function of x, the distance from the mask edge, we have measured the ambipolar diffusion length L_D, of carriers in the channel. From a simple diffusion model, the CL intensity is proportional to $\exp(-x/L_D)$, as first demonstrated by Zarem *et al.*[28] for transport in $GaAs/Al_xGa_{1-x}As$ heterostructures using a similar CL experiment. Our diffusion length experiment was performed for various line scans parallel to and in varying proximity to the DLDs in the samples with 150 and 185 Å $In_{0.2}Ga_{0.8}As$ channel thickness. Owing to the formation of an orthogonal network of dislocations for channel thicknesses greater than 185 Å, we did not attempt this diffusion experiment in samples with thicker $In_{0.2}Ga_{0.8}As$ channels. A nonexponential dependence of the CL intensity would be expected for an e-beam crossing misfit dislocations in this situation, thus requiring more elaborate means to extract the diffusion lengths.

III. RESULTS AND DISCUSSION

A. Evaluation of the average strain relaxation in the HEMT samples

An anisotropy was observed in the density of ⟨110⟩-oriented dislocations, where dislocations first form along $[1\bar{1}0]$ and continue to have a greater density along this direction as the channel thickness increases. The two types of 60° dislocations are chemically inequivalent, owing to the difference in termination of the extra half-plane which, e.g., in the type-I (shuffle) set has a Ga and As termination, respectively, for the unreconstructed α ($[1\bar{1}0]$ line direction) and β ([110] line direction) dislocation cores. For a nonvicinal GaAs(001) substrate (i.e., nominally no misorientation) it is well established that for single thin $In_xGa_{1-x}As$ ($x \lesssim 0.2$) films grown on GaAs(001), α dislocations are the first to form in relaxing the strain.[13,29] This has previously been attributed to the different levels of stress required to nucleate α and β dislocations and the differences in α and β dislocation propagation velocities on nonvicinal GaAs(001) substrates.[30,31] Recently, studies have shown that a misorientation in the GaAs(001) substrate can also affect the degree of the asymmetry in the α and β dislocation density.[14,16,32] Assuming a predominance of 60°-type misfit dislocations in these samples, the average strain relaxation along a ⟨110⟩ direction is 0.02% for a linear dislocation density (LDD) of 1×10^4 cm^{-1}.[29] The maximum in-plane strain of 1.41% in the $In_{0.2}Ga_{0.8}As$ channel is therefore reduced in proportion to the orthogonal LDD. The average [110]- and $[1\bar{1}0]$-oriented LDD and resulting in-plane strains, ϵ_{110} and $\epsilon_{1\bar{1}0}$, are shown in Table I for the HEMT samples with various $In_{0.2}Ga_{0.8}As$ channel thicknesses. The linear dislocation densities were obtained from a combination of CL imaging and plan-view TEM. For CL imaging of DLDs, a maximum area of ~0.4 ×0.4 mm^2 limited by the field of view of the ellipsoidal mirror was used to determine the LDD.

TABLE I. Linear dislocation densities (LDD) along the [110] and $[1\bar{1}0]$ directions for the various $In_{0.2}Ga_{0.8}As$ channel thicknesses. The calculated ϵ_{110} and $\epsilon_{1\bar{1}0}$ strains for each sample are shown.

Channel thickness (Å)	[110] LDD (cm^{-1})	$[1\bar{1}0]$ LDD (cm^{-1})	ϵ_{110}	$\epsilon_{1\bar{1}0}$
75	$<1\times10^1$	$<1\times10^1$	0.014 129	0.014 129
150	3×10^3	$<1\times10^2$	0.014 068	0.014 127
185	5×10^3	4.4×10^2	0.014 027	0.014 120
205	1.7×10^4	5.5×10^2	0.013 785	0.014 117
250	4×10^4	1.8×10^3	0.013 313	0.014 092
300	1.16×10^5	2.5×10^3	0.011 769	0.014 078

In order to evaluate the average strain relaxation in the $In_{0.2}Ga_{0.8}As$ HEMT samples, we have examined spatially integrated CL spectra of these samples at room temperature, as shown in Fig. 2. An area of 128×94 μm^2 was scanned during the acquisition of the these spectra. The energy of the peak position is found to decrease from 1.217 to 1.179 eV as the channel thickness is increased from 150 to 300 Å. The first confined electron to heavy-hole (e1–hh1) transition en-

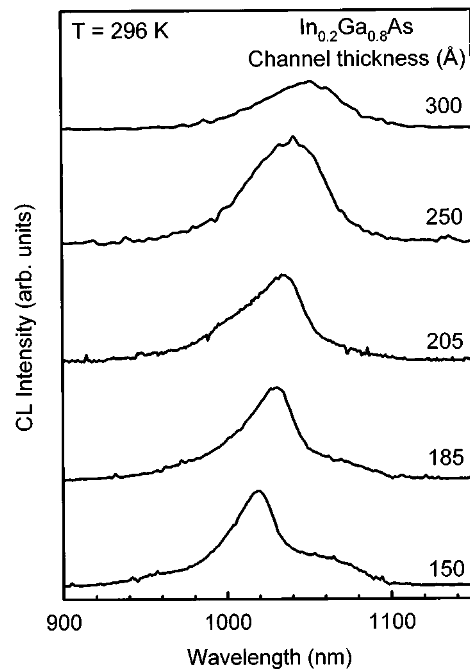

FIG. 2. Stack plot of spatially integrated CL spectra at room temperature for all HEMT samples.

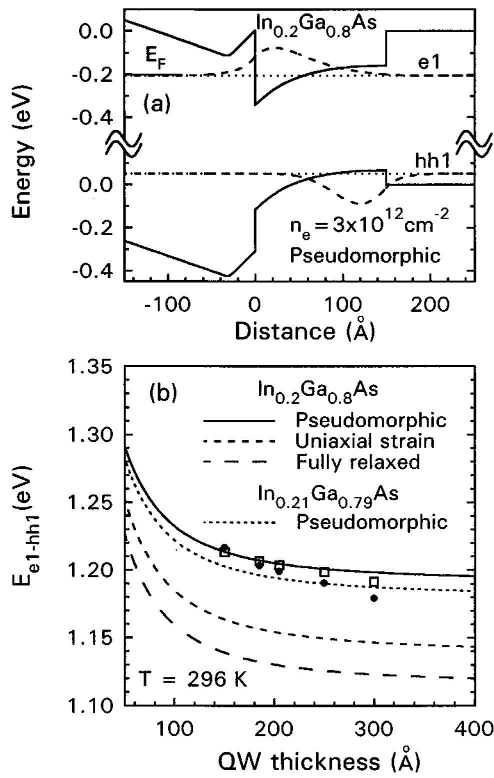

FIG. 3. Self-consistent-field calculation of the band profile for the $In_{0.2}Ga_{0.8}As$ HEMT sample (channel thickness of 150 Å) showing the (a) e1 and hh1 wave functions and Fermi-level position and (b) plots of the theoretical e1–hh1 luminescence energy position vs the $In_{0.2}Ga_{0.8}As$ QW width for the (i) fully strained, (ii) fully relaxed, (iii) uniaxially strained, and (iv) partially relaxed strain (squares) conditions using the data in Table I. The experimental CL peak positions from Fig. 2 are shown with dots in (b). Calculations of e1–hh1 vs the QW width are also shown for a fully strained $In_{0.21}Ga_{0.79}As$ QW, to illustrate the affect of an In composition variation.

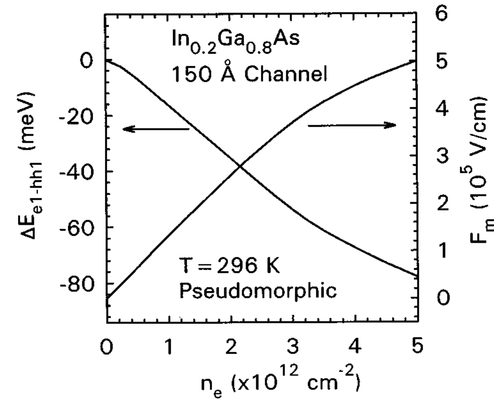

FIG. 4. Self-consistent-field calculation of the maximum electric field F_m in the $In_{0.2}Ga_{0.8}As$ channel and change in the e1–hh1 transition energy vs electron concentration n_e at room temperature.

ergy was calculated as a function of the channel thickness for the cases of

(i) fully biaxially strained (pseudomorphic),
(ii) uniaxially strained,
(iii) fully relaxed, and
(iv) partially relaxed $In_{0.2}Ga_{0.8}As$ channels.

The purpose of the top $Al_{0.25}Ga_{0.75}As$ barrier is to increase the confinement energy for electrons, thereby effectively increasing the electron density in the channel. The resulting asymmetrical QW structure (with a 150 Å width) subject to an electric field created by the ionized δ-doped Si layer is shown in Fig. 3(a).

The electron and hole envelope wave-function calculations were performed with a transfer-matrix method (TMM) technique using a self-consistent-field approximation that includes the Hartree term.[10,33–35] All occupied confined electron states, as determined by the Fermi-level position, were used in calculating the field as a function of position in the channel. A similar method was employed to calculate the field self-consistently in a nipi-doped $In_{0.2}Ga_{0.8}As$ MQW structure, as discussed in Ref. 10. The wave functions and potential were calculated self-consistently using Airy functions in the TMM by discretizing the potential into discrete linear field regions with ~5 Å widths. The use of narrower widths only negligibly affected the calculated electron and hole eigenstates. The conduction to valence-band offset ratios ($\Delta E_c/\Delta E_v$) at both interfaces of the $In_xGa_{1-x}As$ QW were taken as linear interpolations between 70/30 and 60/40 for $GaAs/In_xGa_{1-x}As$ and $GaAs/Al_yGa_{1-y}As$ interfaces, respectively.[36] The results of a calculation showing the band diagram, ground-state electron and hole wave functions, and Fermi level for the pseudomorphic case is shown in Fig. 3(a). The ground-state electron and heavy-hole wave functions are shown superimposed on the calculated band profile in Fig. 3(a). The maximum electric field F_m in the $In_{0.2}Ga_{0.8}As$ channel (for a 150 Å width) and the e1–hh1 transition energy versus the electron concentration in the channel n_e at room temperature is shown in Fig. 4. The maximum field in the channel occurs at the $Al_{0.25}Ga_{0.75}As/In_{0.2}Ga_{0.8}As$ interface, resulting in Stark shifts of the confined electron and hole states. The field-induced Stark shift decreases for a reduced electron concentration in the channel and Si δ-doping concentration, resulting in a larger e1–hh1 transition energy as n_e decreases (as shown in Fig. 4).

The strain-induced changes in the $In_{0.2}Ga_{0.8}As$ band edges were calculated using the 4×4 Luttinger–Kohn and Pikus–Bir Hamiltonian for a general in-plane strain, $\epsilon_{110} \neq \epsilon_{1\bar{1}0}$, referred to the $\langle 110 \rangle$ dislocation directions.[37,38] The strain-induced energy change ΔE of the band gap involving the $j=3/2$ valence bands is given by the following solution of the orbital-strain Hamiltonian for $\mathbf{k}=0$:[15,37]

$$\Delta E = -a(\epsilon_{xx}+\epsilon_{yy}+\epsilon_{zz}) \pm \tfrac{1}{2}\sqrt{4d^2\epsilon_{xy}^2 + b^2(2\epsilon_{zz}-\epsilon_{xx}-\epsilon_{yy})^2 + 3b^2(\epsilon_{xx}-\epsilon_{yy})^2}, \tag{1}$$

where $\epsilon_{xx}=\epsilon_{yy}=(\epsilon_{110}+\epsilon_{1\bar{1}0})/2$, $\epsilon_{xy}=(\epsilon_{1\bar{1}0}-\epsilon_{110})/2$, and $\epsilon_{zz}=-2\epsilon_{xx}C_{12}/C_{11}$; ϵ_{110} and $\epsilon_{1\bar{1}0}$ are the strains along [110] and $[1\bar{1}0]$ directions, respectively. The constant a is the hydrostatic deformation potential; b and d are uniaxial deformation potentials associated with strains of tetragonal and rhombohedral symmetries, respectively, which remove the degeneracy of the bands as indicated by the ± sign; C_{11} and C_{12} are elastic constants; these constants for $In_xGa_{1-x}As$ are found by interpolating between values for GaAs and InAs.[38,39] The low symmetry of a $\epsilon_{110}\neq\epsilon_{1\bar{1}0}$ strain in the $In_{0.2}Ga_{0.8}As$ channel required the use of the Luttinger–Kohn Hamiltonian to determine the $In_{0.2}Ga_{0.8}As$ effective mass of holes along the [001] growth direction. Standard hole masses and band gaps are used for $Al_xGa_{1-x}As$. The Luttinger parameters are taken as a linearization, again, between the values for InAs and GaAs.[38] The effective masses and strain-modified barrier heights were then used in the TMM calculation to calculate the e1–hh1 transition energies for

(i) the pseudomorphic case ($\epsilon_{110}=\epsilon_{1\bar{1}0}=0.0141$),
(ii) the uniaxial strain condition ($\epsilon_{110}=0$ and $\epsilon_{1\bar{1}0}=0.0141$),
(iii) the fully relaxed case ($\epsilon_{110}=\epsilon_{1\bar{1}0}=0$), and
(iv) the partially relaxed case with general strain values, ϵ_{110} and $\epsilon_{1\bar{1}0}$, as obtained from the measured dislocation densities shown in Table I for each channel thickness.

The results are shown in Fig. 3(b) as solid lines, medium-dashed lines, long-dashed lines, and squares for cases (i)–(iv), respectively. The experimental e1–hh1 peak energies (dots) are found to lie closest to the theoretical curve for the pseudomorphic case ($\epsilon_{110}=\epsilon_{1\bar{1}0}=0.0141$).

The deviation between the experimental peak positions and pseudomorphic calculation increases as the channel thickness increases, consistent with an increased strain relaxation of the $In_{0.2}Ga_{0.8}As$ channel. The use of the measured strains of Table I resulted in a better agreement between the experimental and calculated e1–hh1 transition energies, as shown in Fig. 3(b). The CL imaging and plan-view TEM revealed an increase in the dislocation density with increasing channel thickness as shown in Table I. It is apparent that even for the case of the largest channel width of 300 Å, the largest dislocation density yields a strain of $\epsilon_{110}=0.0118$, and the film is still ~84% strained in the [110] direction. Therefore, the TMM calculations, when incorporating the observed strain relaxation, explain the salient features of the CL peak energies for varying channel thicknesses. Further, the deviation between the experiment and calculations for the partially relaxed case [dots and squares, respectively, in Fig. 3(b)] is likely due to a variation in the In composition x. A calculation of the e1–hh1 energy for a fully strained $In_{0.21}Ga_{0.79}As$ QW (short-dashed lines) is shown in Fig. 3(b), indicating a ~10 meV decrease in the calculated e1–hh1 energy will occur for cases (i) and (iv) above if $x=0.21$ is used instead of $x=0.20$ in these calculations.

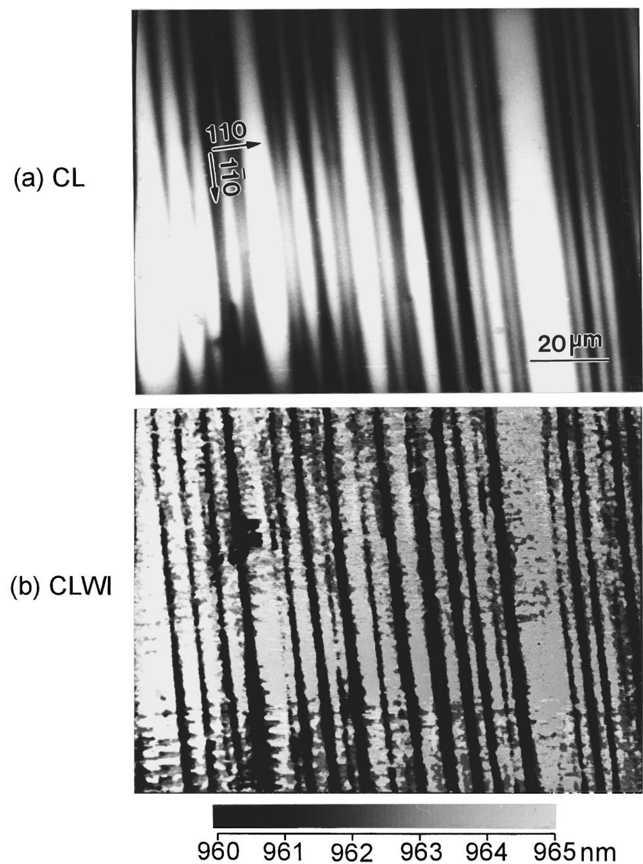

FIG. 5. (a) CL intensity and (b) CLWI images of the same regions in the $In_{0.2}Ga_{0.8}As$ HEMT sample with 150 Å channel thickness.

B. Local CL energy and polarization variations in close proximity to dislocations

Recently, we have established that there are significant energy and polarization variations in the optical transitions in close proximity to misfit dislocations, in addition to the nonradiative behavior of DLDs.[14–16] The previous systems examined were partially relaxed $In_xGa_{1-x}As$/GaAs films which had linear dislocations densities greater than $\sim1\times10^4$ cm^{-1} or one dislocation per μm. Since the carrier diffusion length is ~1 μm, defect densities greater than 1×10^4 cm^{-1} result in DLDs that are composed of bunches of dislocations, which cannot be resolved individually with conventional CL imaging. Bunches of dislocations that are formed with very narrow dislocation spacings can result in nearly complete strain relaxation along one ⟨110⟩ direction with a partial strain remaining in the orthogonal direction. This can further result in a quasi-uniaxial stress leading to a large $I_\parallel/I_\perp$ polarization anisotropy and a reduction in the excitonic transition energy, as previously reported.[14–16]

We have pursued a similar analysis here for the case of dislocations separated by a length on average greater than the carrier diffusion length, so as to examine the effects of isolated dislocations. Figures 5 and 6 show (a) CL intensity and (b) CLWI images of samples with 150 and 185 Å channel thicknesses, respectively. The false-color scale represents the

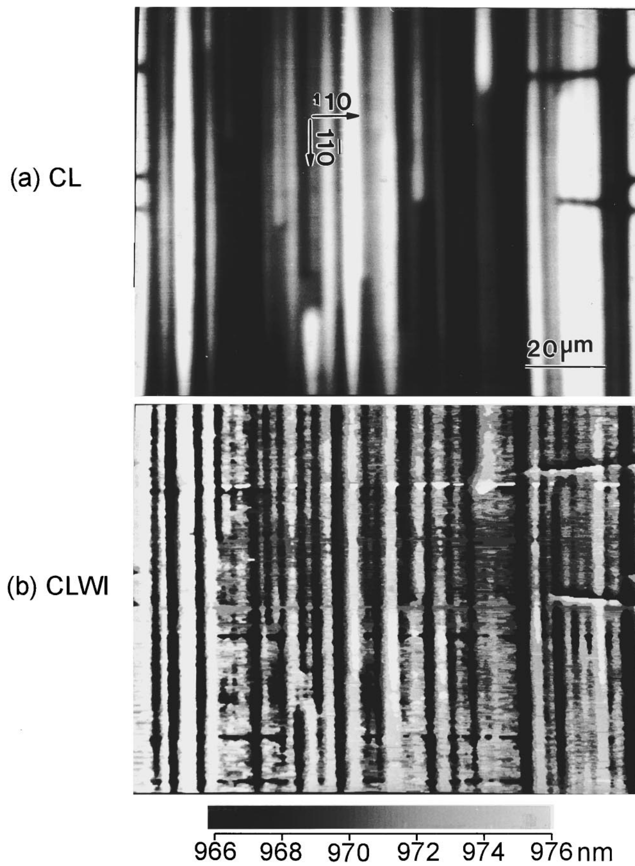

FIG. 6. (a) CL intensity and (b) CLWI images of the same regions in the $In_{0.2}Ga_{0.8}As$ HEMT sample with 185 Å channel thickness.

wavelength position λ_m of the peak CL intensity. A particularly striking feature is observed in the CLWI images. The wavelength of emission is found to decrease near the DLD position, showing a blue shift correlated with a defect-induced CL intensity reduction. Figures 7 and 8 each show a line scan analysis for an arbitrary line scan taken perpendicular to the $[1\bar{1}0]$ dislocation direction and illustrate a one-to-one correlation between the blue shift and the DLD position. A maximum increase of ~5 and ~10 meV is seen at the DLD centers for the 150 and 185 Å samples, respectively, in Figs. 5–8. This behavior appears contradictory to the previously observed red shift measured near DLD positions in $In_xGa_{1-x}As$ samples exhibiting a greater strain relaxation and greater dislocation-induced reductions in the ϵ_{110} strain.[14–16] This apparent discrepancy is, however, explained by the influence of the dislocations and associated point defects on the electron density in the channel. It is our hypothesis that these defects create localized deep levels and traps that reduce the effective electron density in the channel near DLDs, thereby simultaneously reducing the field in the channel. The reduction in both the electron density and field will concomitantly reduce the Stark shift, thereby resulting in a local increase in the e1–hh1 emission energy. A similar behavior was observed for defect-induced reductions in the electric field and Stark shifts for nipi-doped $In_{0.2}Ga_{0.8}As/GaAs$ MQWs.[10] The larger blue shift in the e1–

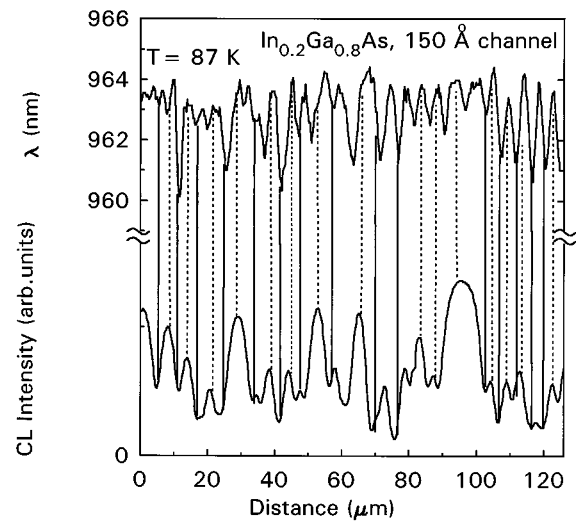

FIG. 7. Line scan analysis for an arbitrary [110]-oriented line for the images of Fig. 5 (150 Å $In_{0.2}Ga_{0.8}As$ channel width) showing the CL intensity and CLWI position correlations. Dashed and solid vertical lines are used to show correlations between a reduced CL intensity (DLDs) and a blue shift in the e1–hh1 transition energy.

hh1 transition energies for the 185 Å sample (Figs. 6 and 8) is evidently due to the enhanced dislocation density. Dislocation bunching and an enhanced point defect density are more prevalent for larger $In_{0.2}Ga_{0.8}As$ channel thicknesses, which should result in a greater local depletion of the electron density in the channel.

The local strain relaxation appears to minimally effect the e1–hh1 transition energy. As shown in Fig. 3, the curve for a uniaxial strain condition is ~50 meV lower than that for the pseudomorphic case. A defect-induced reduction in the quan-

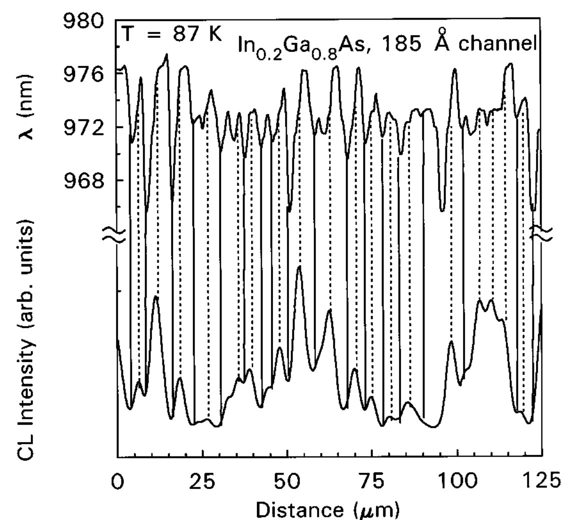

FIG. 8. Line scan analysis for an arbitrary [110]-oriented line for the images of Fig. 6 (185 Å $In_{0.2}Ga_{0.8}As$ channel width) showing the CL intensity and CLWI position correlations. Dashed and solid vertical lines are used to show correlations between a reduced CL intensity (DLDs) and a blue shift in the e1–hh1 transition energy.

tum confined Stark effect could also cause a blue shift of ~50 meV in the e1–hh1 transition energy, as seen from Fig. 4. That is, strain relaxation and defect-induced reductions in the field cause the e1–hh1 energy to shift in opposite directions, thereby possibly masking the effects caused by strain relaxation. However, from the CL polarization results discussed below, we show that the average strain tensor within the ~1 μm carrier diffusion length near DLDs is still well described by a biaxial strain with $\epsilon_{110} \approx \epsilon_{1\bar{1}0}$, for the 150 and 185 Å samples analyzed in Figs. 5–8.

Linearly polarized monochromatic CL images were taken with the polarizer rotated to detect emission of light with $\mathbf{E}\perp[110]$ and $\mathbf{E}\|[110]$ detection orientations at wavelengths of 962 and 972 nm for the 150 and 185 Å samples, respectively. In order to emphasize the polarization variations, the ratio of these images is displayed in Figs. 9 and 10. The pixels in the ratio image at a (x,y) position are presented as $\log[I_\perp(x,y)/I_\|(x,y)]$, where $I_\perp$ and $I_\|$ are the pixel intensities under $\mathbf{E}\perp[110]$ and $\mathbf{E}\|[110]$ detection orientations. The bright and dark bands present in the LPCL ratio images exhibit a local polarization anisotropy, which indicates the presence of μm-scale variations in ϵ_{110}. These bands correlate with the peaks and dips in the CL intensity image, as shown in the line scan analysis of Fig. 11 for the 185 Å sample. The maximum polarization anisotropies (minimum ratios) are $I_\perp/I_\| \approx 0.95$ and $I_\perp/I_\| \approx 0.85$ for the 150 and 185 Å samples, respectively. The spatially averaged $I_\perp/I_\|$ ratios for the LPCL images of Figs. 9(b) and 10(b) are 0.98 and 0.95, respectively. From the four-band $\mathbf{k}\cdot\mathbf{p}$ calculation discussed above, we have calculated $I_\perp/I_\|$ using the dipole approximation in Fermi's golden rule, i.e., $I_{\perp,\|} \propto |\langle u_e|\mathbf{E}_{\perp,\|}\cdot\mathbf{p}|u_h\rangle|^2$, where u_e is the electron wave function, u_h is the wave function of the uppermost hole state, and $\mathbf{p}$ is the linear momentum operator. Both u_e and u_h include the envelope wave functions and zone-center Bloch functions for the s- and p-type conduction- and valence-band states, respectively. The polarization ratio was calculated for a fixed $\epsilon_{1\bar{1}0} = 0.0141$ and variable ϵ_{110}, to simulate the effect of a transition from uniaxial to biaxial (pseudomorphic) strain. The results are shown in Fig. 12 for the 150 and 185 Å samples, where we also show the calculated e1–hh1 transition energy as a function of ϵ_{110}. From the measured average polarization anisotropy ratios above and the calculation in Fig. 12, the estimated values for ϵ_{110} are 0.0138 and 0.0132 (i.e., 98% and 94% strained) for the 150 and 185 Å samples, respectively. This is in reasonable agreement with the low strain relaxation and ϵ_{110} values observed in Table I from the linear dislocation densities for these samples. These results contrast with the situation previously studied for highly relaxed $In_xGa_{1-x}As$ samples with dislocation densities greater than $\sim 1\times10^5$ cm^{-1}, where dislocation bunching lead to a quasiuniaxial strain and a larger polarization anisotropy.[14–16] Thus, for individual dislocations studied here, within the minority carrier diffusion length of ~1 μm, the presence of dislocations with densities less than $\sim 1\times10^4$ leads to a measured luminescence behavior still well described by a biaxial strain, $\epsilon_{110} \approx \epsilon_{1\bar{1}0}$.

C. The CL temperature dependence and spatial variations in the activation energy

The integrated CL intensity I_T of the e1–hh1 transition in the $In_{0.2}Ga_{0.8}As$ channel and the excitonic luminescence of the $GaAs/Al_{0.25}Ga_{0.75}As$ MQW was measured as a function of temperature for selected local regions in close proximity to and away from dislocations, labeled D and B, respectively to denote dark and bright regions in the $In_{0.2}Ga_{0.8}As$ CL imaging. The results are shown in Fig. 13 for both the 150 and 185 Å samples in a log I_T vs 1000/T plot. The CL intensities reduce as the temperature increases from 87 to 250 K. This reduction corresponds to the increase of thermally activated nonradiative recombination, which causes an Arrhenius dependence in the high-temperature range. In previous reports of the temperature-dependent luminescence efficiency,[17,18,40] the linear region of the Arrhenius behavior in the high-temperature range was characterized by one or two thermally activated nonradiative recombination processes. We use the following fitting equation for the temperature dependence of the $In_{0.2}Ga_{0.8}As$ QW CL intensity:

$$I_T = R\eta, \tag{2}$$

where $\eta = 1/(1+R_{nr}/R_r)$ is the quantum efficiency,[41,42] R is a coefficient which depends on the generation rate of electron–hole pairs and the relative weights of monomolecular and bimolecular recombination,[41] R_r is the radiative recombination rate which is assumed to be temperature independent, and R_{nr} represents the rate for nonradiative recombination and is assumed to have the following temperature dependence:

$$R_{nr} = R_{nr1} + R_{nr0}\exp(-E_a/kT), \tag{3}$$

where R_{nr0} and E_a are the temperature-independent prefactor and the thermal activation energy,[40,42] respectively, and R_{nr1} is the rate for nonthermally activated nonradiative recombination (i.e., independent of temperature). The temperature-dependent exponential term is due to the enhancement of the capture cross section of nonradiative recombination centers as seen by carriers as the temperature increases. The model of Eq. (3) is motivated by the existence of DLDs in the CL imaging at the lowest temperatures, indicating that there are nonradiative channels which are independent of any thermal activation. Therefore,

$$I_T = \frac{\theta}{1+\beta\exp(-E_a/kT)}, \tag{4}$$

where $\theta = R/(1+R_{nr1}/R_r)$ and $\beta = R_{nr0}/(R_r+R_{nr1})$ are independent of temperature and depend on the density of nonthermally and thermally activated nonradiative recombination centers. At the low-temperature limit, η saturates since thermally activated nonradiative recombination vanishes and $I_T = \theta$. The spatial variation in θ therefore accounts for the difference in I_T, the e1–hh1 emission intensity, when $T \lesssim 100$ K, as shown in Figs. 9, 10, and 13. The solid lines in Fig. 13 show a fit of Eq. (4) to the experimental CL data for the e1–hh1 transition at the corresponding B (bright) and D

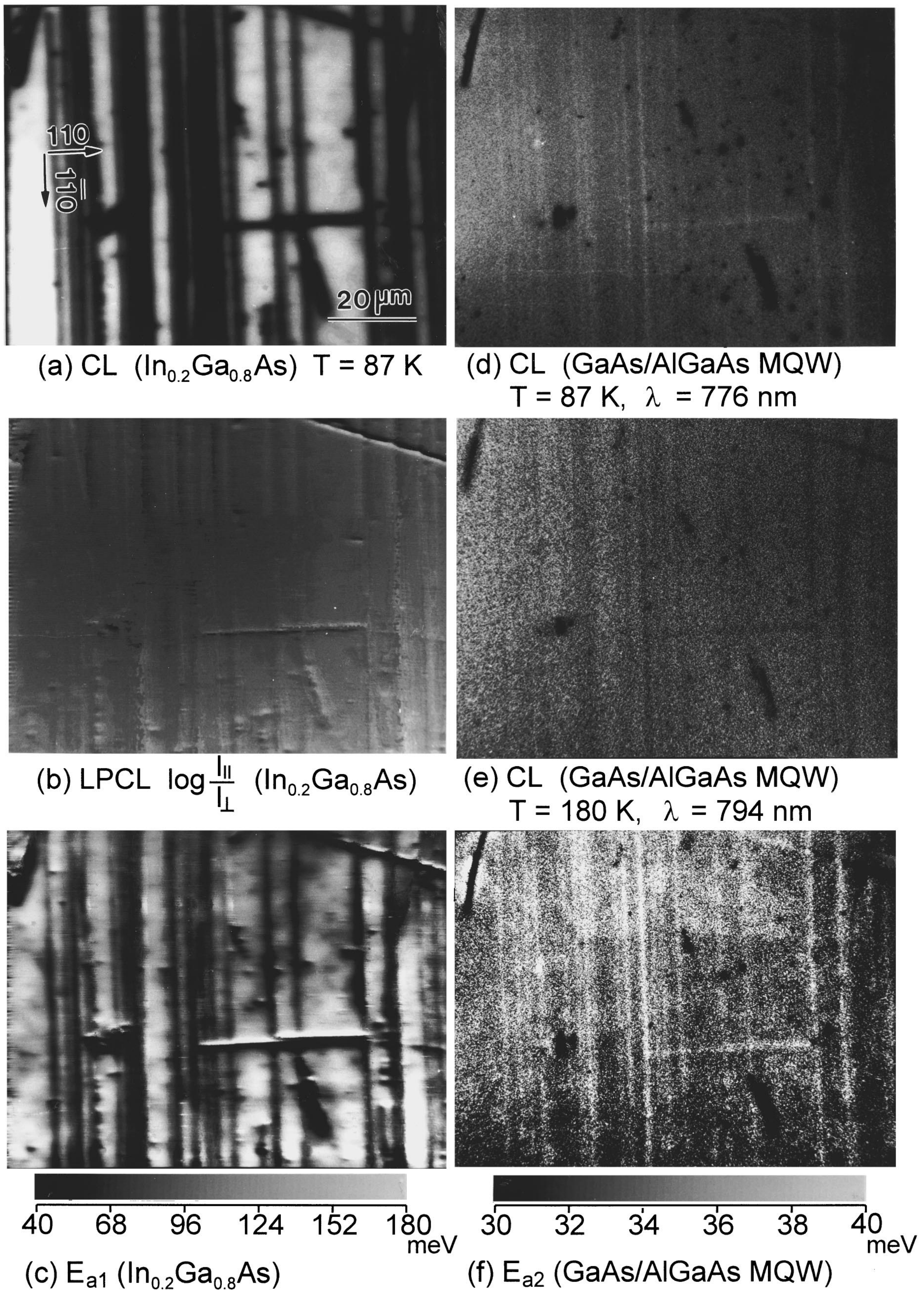

FIG. 9. CL imaging of the 150 Å $In_{0.2}Ga_{0.8}As$ HEMT sample showing (a) spectrally integrated CL intensity images for the e1–hh1 emission, (b) LPCL $I_{\perp}/I_{\parallel}$ ratio images, (c) activation energy E_{a1} images for the $In_{0.2}Ga_{0.8}As$ QW luminescence, monochromatic CL images for $GaAs/Al_{0.25}Ga_{0.75}As$ MQW at (d) $T=87$ K and (e) 180 K, and (f) activation energy E_{a2} images for the $GaAs/Al_{0.25}Ga_{0.75}As$ MQW emission.

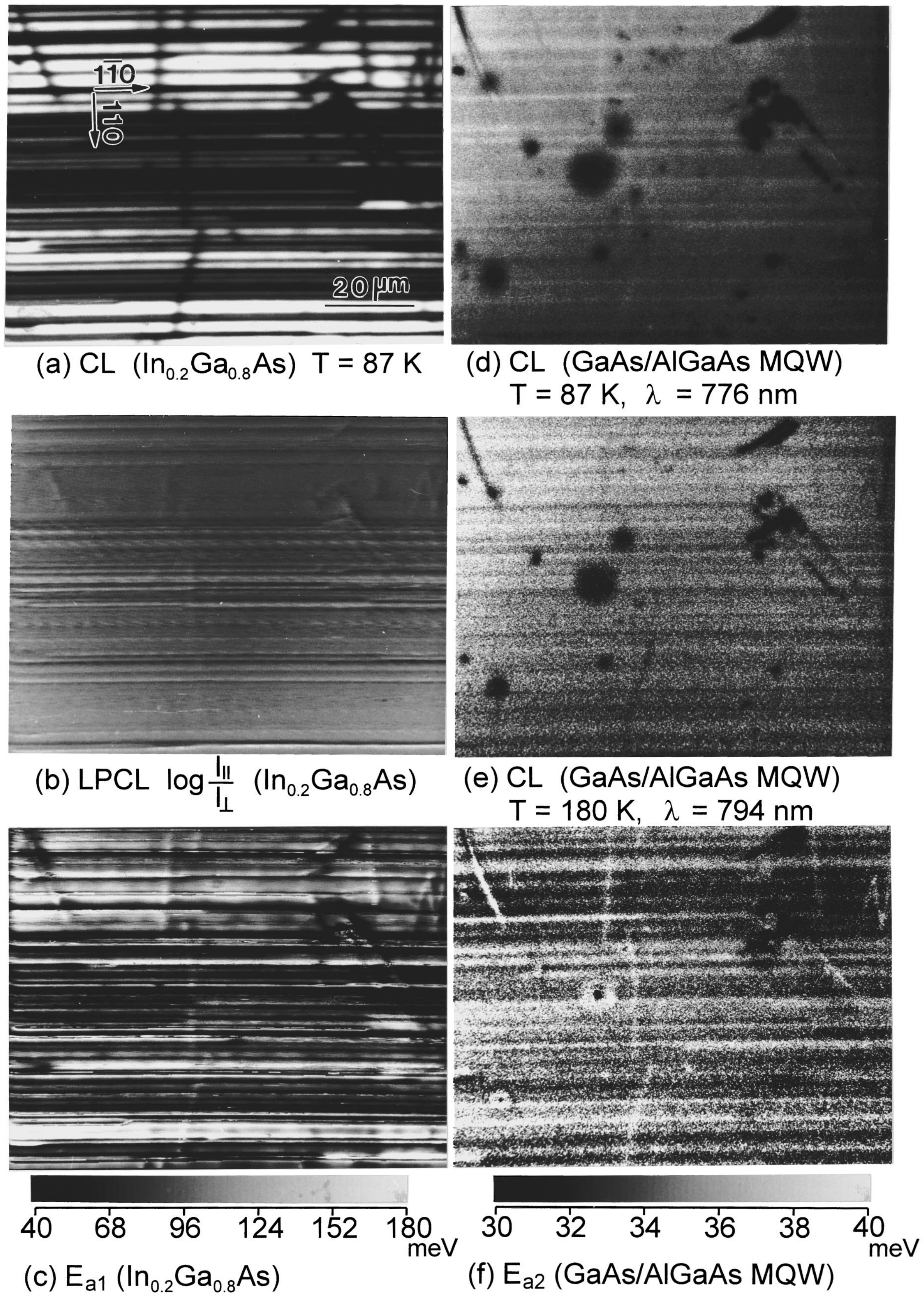

FIG. 10. CL imaging of the 185 Å $In_{0.2}Ga_{0.8}As$ HEMT sample showing (a) spectrally integrated CL intensity images for the e1–hh1 emission, (b) LPCL $I_{\perp}/I_{\parallel}$ ratio images, (c) activation energy E_{a1} images for the $In_{0.2}Ga_{0.8}As$ QW luminescence, monochromatic CL images for $GaAs/Al_{0.25}Ga_{0.75}As$ MQW at (d) $T=87$ K and (e) 180 K, and (f) activation energy E_{a2} images for the $GaAs/Al_{0.25}Ga_{0.75}As$ MQW emission.

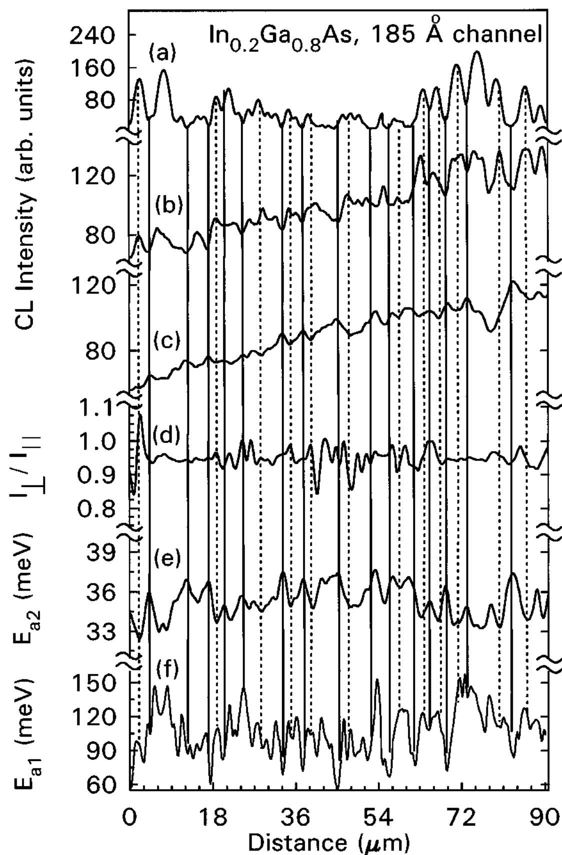

FIG. 11. Line scan analysis for an arbitrary [110]-oriented line for the images of Fig. 10 (185 Å $In_{0.2}Ga_{0.8}As$ channel width) showing (a) the CL intensity for the e1–hh1 emission, $GaAs/Al_{0.25}Ga_{0.75}As$ MQW emission intensity at (b) $T=180$ K and (c) 87 K, (d) LPCL $I_\perp/I_\parallel$ ratio, and activation energies (e) E_{a2} and (f) E_{a1}.

(dark) regions. The activation energies E_{a1}, were determined for each pixel position by fitting all 640×480 pixel intensity values for the monochromatic CL images of the e1–hh1 transition taken at 12 different temperatures. The results of E_{a1} for each (x,y) position are shown in Figs. 9(c) and 10(c), for

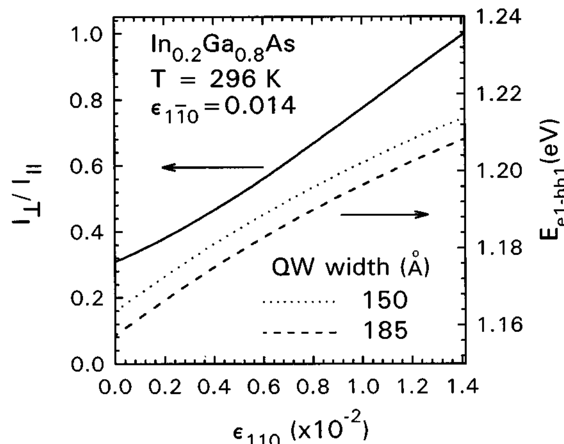

FIG. 12. Calculation of the e1–hh1 $I_\perp/I_\parallel$ emission ratio and $In_{0.2}Ga_{0.8}As$ QW transition energy vs ϵ_{110} for a fixed $\epsilon_{1\bar{1}0} = 0.0141$ at room temperature.

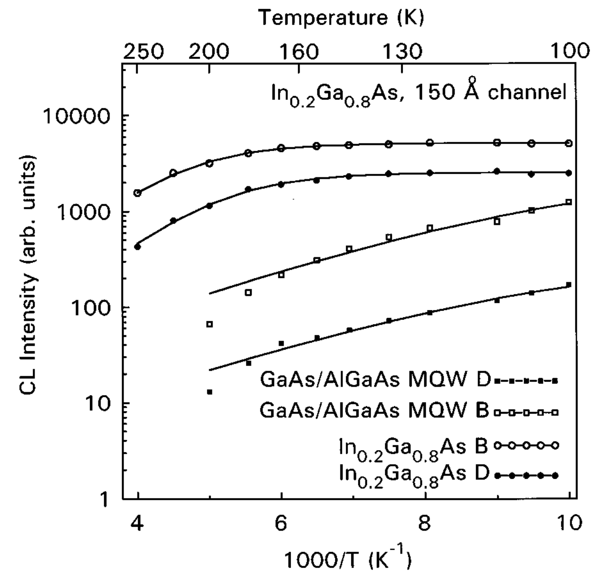

FIG. 13. CL intensity vs 1000/T for the same local bright (B) and dark regions (D) in the $In_{0.2}Ga_{0.8}As$ e1–hh1 and $GaAs/Al_{0.25}Ga_{0.75}As$ MQW monochromatic CL images. The solid lines running through the curves are a fit of Eq. (4) to the data to determine the activation energies E_{a1} and E_{a2} for the $In_{0.2}Ga_{0.8}As$ QW and $GaAs/Al_{0.25}Ga_{0.75}As$ MQW luminescence, respectively.

the 150 and 185 Å samples, respectively. A line scan analysis is also shown in Fig. 11(f) for the 185 Å sample.

For the luminescence originating from the $GaAs/Al_{0.25}Ga_{0.75}As$ MQW, I_B, a low-temperature saturation of its intensity was not reached for the 87 K minimum in this study (as shown in Fig. 13). We have also fit the CL images of I_B, taken at the 12 different temperatures, with the model of Eqs. (2)–(4), obtaining the activation energy, E_{a2} for the $GaAs/Al_{0.25}Ga_{0.75}As$ MQW excitonic luminescence. The results of two fits are shown by the solid lines in the log plot of Fig. 13 for the same regions, B and D, as indicated for the e1–hh1 $In_{0.2}Ga_{0.8}As$ luminescence. We further observe a change in the relative intensity of the $GaAs/Al_{0.25}Ga_{0.75}As$ MQW emission near features which correspond to DLDs in the CL imaging of the e1–hh1 $In_{0.2}Ga_{0.8}As$ QW emission. At $T=180$ K, for both the 150 and 185 Å samples, the imaging of the $GaAs/Al_{0.25}Ga_{0.75}As$ MQW emission [Figs. 9(e) and 10(e)] results in DLDs which correlate, one to one, with that of the e1–hh1 imaging, as also shown in the line scan data of Fig. 11. As the temperature is lowered, a reversal in the relative intensity of the $GaAs/Al_{0.25}Ga_{0.75}As$ MQW emission occurs near defects, resulting in bright lines in the CL images, as shown in Figs. 9(d) and 10(d). This striking contrast reversal is also illustrated in the line scan analysis of Figs. 11(b) and 11(c). That is, high-temperature DLDs in the $GaAs/Al_{0.25}Ga_{0.75}As$ MQW emission become bright line defects (BLDs) at lower temperatures. The activation energy for this emission E_{a2} increases near these defects, as indicated by the imaging and line scan analysis. This is in contrast to the decrease in E_{a1} near DLDs.

This behavior reflects salient differences in the thermal

activation of carriers which are in close proximity, but on opposite sides, of the $In_{0.2}Ga_{0.8}As$/GaAs interface. The E_{a1} energy represents the activation energy for thermal reemission of carriers out of the $In_{0.2}Ga_{0.8}As$ QW, as has been observed for similar QW and MQW systems.[17–20] Once out of the $In_{0.2}Ga_{0.8}As$ QW, the carriers can be recaptured by the QW, recombine in the GaAs barrier, or diffuse to the GaAs/$Al_{0.25}Ga_{0.75}As$ MQW where recombination can occur. An extremely weak GaAs near-band-edge luminescence was detected relative to emissions from the $In_{0.2}Ga_{0.8}As$ QW and GaAs/$Al_{0.25}Ga_{0.75}As$ MQW, indicating the very low impurity concentration and high quality of the GaAs barrier layer. Carriers which are generated in the GaAs barrier will then primarily diffuse to the underlying GaAs/$Al_{0.25}Ga_{0.75}As$ MQW or $In_{0.2}Ga_{0.8}As$ QW, where a higher carrier capture rate in these layers is expected, owing to quantum capture. The 3000 Å thickness of the GaAs barrier is less than the ~1 μm ambipolar diffusion length for high-quality and low-impurity GaAs, thereby enabling the GaAs barrier to serve as a conduit for efficient transport of electrons and holes to and from the GaAs/$Al_{0.25}Ga_{0.75}As$ MQW and $In_{0.2}Ga_{0.8}As$ QW.

The defects created by the misfit dislocations further introduce other recombination channels for carriers in the $In_{0.2}Ga_{0.8}As$ QW. These defects enhance the probability for thermally assisted nonradiative recombination for carriers already residing in the $In_{0.2}Ga_{0.8}As$ QW, thereby resulting in a decrease in E_{a1} near DLDs. The analysis in Figs. 9(c), 10(c), and 11(f) shows that there is a maximum decrease in E_{a1} of ~60 and ~80 meV near DLDs for the 150 and 185 Å samples. The greater reduction in E_{a1} for the 185 Å sample reflects the enhanced defect density.

For carriers recombining in the GaAs/$Al_{0.25}Ga_{0.75}As$ MQW, the misfit dislocations, likewise, introduce additional thermally assisted nonradiative channels which are accessible at higher temperatures. These channels may compete with carrier capture by the $In_{0.2}Ga_{0.8}As$ QW and subsequent radiative recombination. However, at lower temperatures, carrier capture by these defects is substantially reduced and simultaneously results in a reduced transfer of carriers from the GaAs/$Al_{0.25}Ga_{0.75}As$ MQW to the $In_{0.2}Ga_{0.8}As$ QW at defect sites, thereby resulting in a local increase of E_{a2}. These defect sites also appear to act as a barrier to transport into the $In_{0.2}Ga_{0.8}As$ QW at low temperatures, thereby enhancing the relative GaAs/$Al_{0.25}Ga_{0.75}As$ MQW emission near dislocations and resulting in BLDs correlated with the $In_{0.2}Ga_{0.8}As$ DLDs. The spatially averaged values of E_{a2} [from Figs. 9(f) and 10(f)] are 32.3 and 35.3 meV for the 150 and 185 Å samples. The larger value in the latter sample again likely reflects the larger relaxation-induced defect density in that sample.

D. Spatial variations in the carrier diffusion length

The diffusion length experiment was performed by scanning the e beam along the [1$\bar{1}$0] direction (parallel to the DLDs) and recording the intensity of the e1–hh1 luminescence as a function of the distance x from the mask edge (as illustrated in Fig. 1). Typical scans are shown for the 150 and 185 Å $In_{0.2}Ga_{0.8}As$ samples at four different regions in each sample, labeled a–d, in Fig. 14. These regions are further identified in the CL line scan analysis of Figs. 15 and 16, which show the $In_{0.2}Ga_{0.8}As$ QW luminescence intensity versus distance (bottom scan) along [110] (i.e., perpendicular to the dislocation line direction). The dips in the CL intensity scan, again, represent the DLDs. For both samples, regions a and b are away from DLDs, while c and d are near the center of DLDs. From Fig. 14 it is apparent that a reduction in CL intensity at these regions is also accompanied by a greater negative slope, resulting in a smaller ambipolar diffusion length. This correlation is illustrated in Figs. 15 and 16 for several diffusion length measurements performed in varying proximity to DLDs at different temperatures. For both samples, regions near and far from the DLDs correspond to regions of smaller and larger diffusion lengths, respectively. A wide variation in L_D is observed from about 0.5 to 3 μm in Fig. 17, showing that defect regions can substantially influence the transport. No clear systematic variations in L_D with temperature are observed.

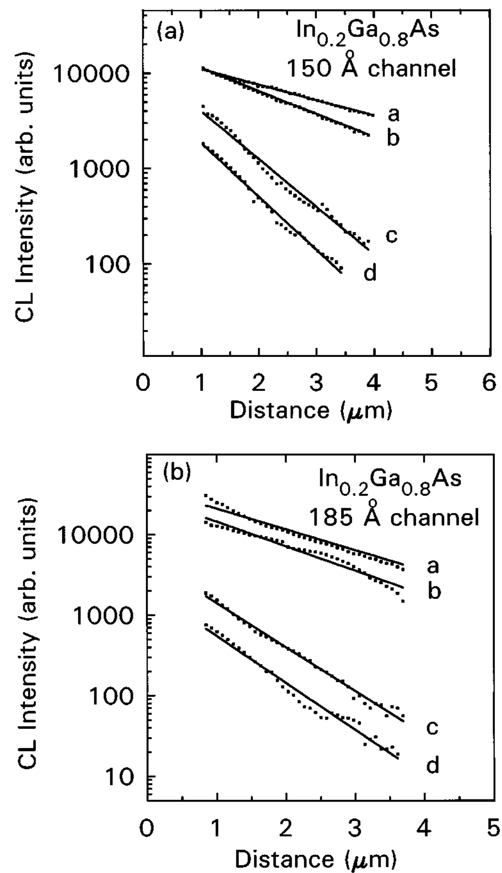

FIG. 14. CL intensity vs beam position x for different line scans (labeled a–d) parallel to the [1$\bar{1}$0] dislocation line direction near and between DLDs for both the 150 and 185 Å $In_{0.2}Ga_{0.8}As$ HEMT samples.

From previous Hall measurements of these samples, the $In_{0.2}Ga_{0.8}As$ channel contains a large electron concentration of $\sim 3\times 10^{12}$ cm^{-2} at 77 K.[21,22] The L_D measured here therefore reflects the diffusion of the minority carriers, i.e., holes.

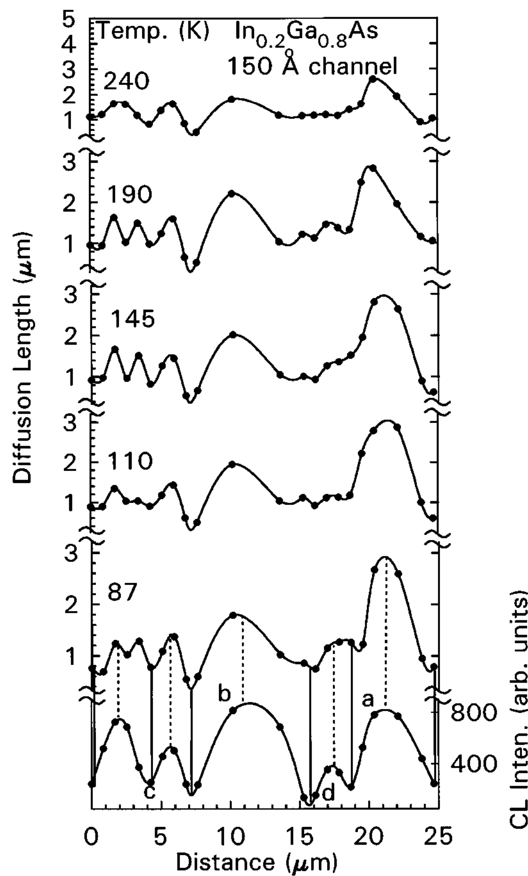

FIG. 15. CL intensity and diffusion length plot vs distance along [110] (perpendicular to the dislocation direction) for various temperatures for the 150 Å sample. The dashed and solid vertical lines show the spatial correlations between the DLD positions and a reduced diffusion length.

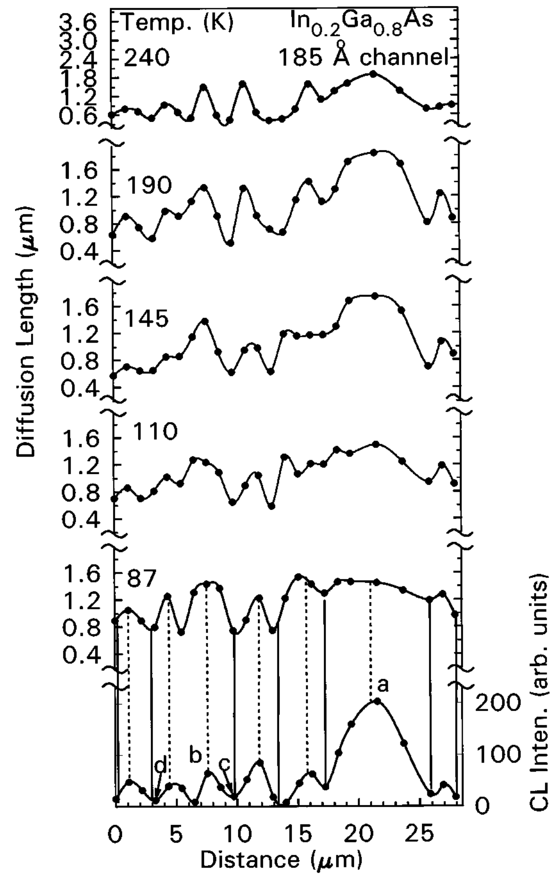

FIG. 16. CL intensity and diffusion length plot vs distance along [110] (perpendicular to the dislocation direction) for various temperatures for the 185 Å sample. The dashed and solid vertical lines show the spatial correlations between the DLD positions and a reduced diffusion length.

This hole diffusion length will involve an interplay between local changes in mobility μ_p, and minority-carrier recombination lifetime τ_p as $L_D=(D_p\tau_p)^{1/2}$, where μ_p and D_p are related by the Einstein relation $\mu_p=eD_p/kT$.[43] The presence of defects will evidently reduce both μ_p and τ_p as a result of enhanced scattering near defects and introduction of nonradiative recombination channels. As discussed in Sec. III A, the enhanced defect density near dislocations is expected to locally reduced the electric field. The reduction in the field is also expected to result in a decrease in τ_p since the electron and hole envelope wave-function overlap will also increase with a decrease in the field [see Fig. 3(a)]. However, without a quantitative measurement of the lifetime and its variations we refrain from attempting to deconvolve L_D into separate μ_p and τ_p terms here.

IV. SUMMARY AND CONCLUSIONS

A detailed study of fundamental optical and transport properties of two $In_{0.2}Ga_{0.8}As$ HEMT samples has been performed for channel thicknesses that just exceed the $In_{0.2}Ga_{0.8}As$ critical thickness. This facilitated a study of the excitonic luminescence polarization and wavelength, thermally activated nonradiative recombination, and carrier diffusion in a strain relaxation regime where the optical and transport properties near individual dislocations were examined. The dislocations and DLD network were found well separated on a μm scale and oriented primarily along one of the ⟨110⟩ directions. A plan-view TEM and CL imaging analysis was used to determine the linear dislocation densities for a greater range of samples with $In_{0.2}Ga_{0.8}As$ channel thicknesses below and well beyond the critical thickness. Theoretical calculations using a four-band $\mathbf{k}\cdot\mathbf{p}$ and TMM were used to calculate the band profile and eigenstates of the HEMT samples. The electric field in the channel and the electron and hole eigenstates were treated self-consistently. CL wavelength imaging showed a striking blue shift of ~5 and ~10 meV in the 150 and 185 Å samples, respectively, contrary to a previous red shift observed in undoped samples which exhibited a greater strain relaxation, as reported in Refs. 14–16. We hypothesize that a defect-induced reduction in the field occurs and leads to a reduced Stark shift of the electron and hole eigenstates.

A small polarization anisotropy is observed, consistent with the level of strain relaxation in each sample and theoretical calculations of the polarization ratio. The activation energies for the $In_{0.2}Ga_{0.8}As$ QW and $GaAs/Al_{0.25}Ga_{0.75}As$ MQW luminescence were obtained by temperature-

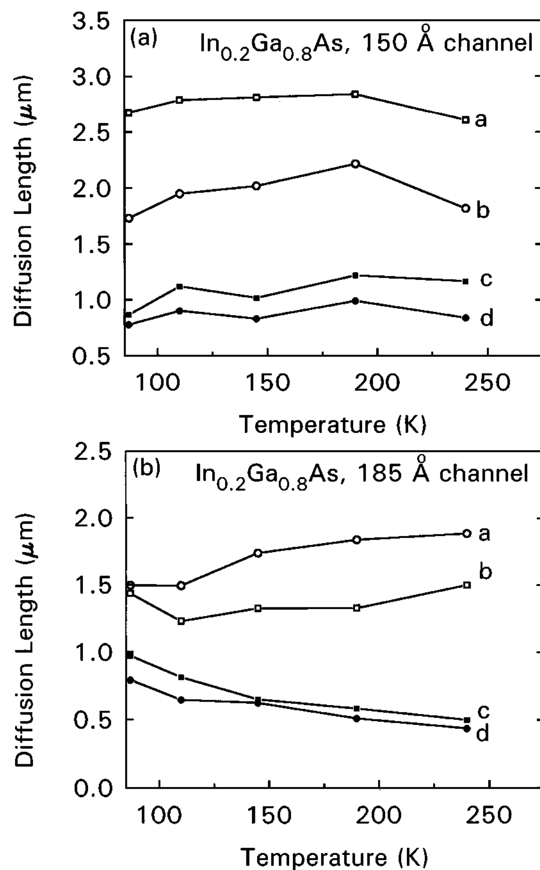

FIG. 17. Diffusion length vs temperature for various bright (a and b) and dark (c and d) regions in both 150 and 185 Å samples.

dependent CL measurements. Spatial variations in the activation energies are found to correlate with DLDs. These defects were found to lower the activation energy for thermal reemission of carriers from the $In_{0.2}Ga_{0.8}As$ QW and increase the activation energy for carrier transfer into the $In_{0.2}Ga_{0.8}As$ QW from the underlying GaAs barrier and $GaAs/Al_{0.25}Ga_{0.75}As$ MQW. The ambipolar diffusion length of carriers in the $In_{0.2}Ga_{0.8}As$ QW was quantified with a noncontact optical diffusion length measurement which utilized a one-dimensional line scan during monochromatic CL detection and a Ag mask which covered part of the sample. The diffusion lengths of holes parallel to the dislocation line direction were found to decrease by as much as a factor of ~5 in close proximity to DLDs, thereby revealing that an important transport parameter is deleteriously effected by the dislocation formation. Future time-resolved CL measurements involving lifetime determinations on a μm scale should help clarify the competing roles of mobility and the minority-carrier lifetime in determining the diffusion lengths. This study revealed that the optical and transport properties of $In_xGa_{1-x}As$ HEMTs are linked on a μm scale and are both intimately tied to the presence of misfit dislocations and dark line defects which form during strain relaxation.

ACKNOWLEDGMENTS

The work performed at USC was supported by the U.S. Army Research Office and the National Science Foundation (RIA-ECS). The research performed at UCLA was supported through funding from TRW, the UC MICRO Program, the National Science Foundation, and the National Defense Science and Engineering Graduate Fellowship Program. The authors thank D. C. Streit, T. R. Block and M. Wojtowicz of TRW, Electronic Technology Division, and Space and Electronics Group in Redondo Beach, CA for use of their HEMT samples.

[1] N. Moll, M. R. Hueschen, and A. Fischer-Colbrie, IEEE Trans. Electron Devices **ED-35**, 878 (1988).
[2] L. D. Nguyen, D. C. Radulescu, M. C. Foisy, P. J. Tasker, and L. F. Eastman, IEEE Trans. Electron Devices **ED-36**, 833 (1989).
[3] A. Fischer-Colbrie, J. N. Miller, S. S. Laderman, S. J. Rosner, and R. Hull, J. Vac. Sci. Technol. B **6**, 620 (1988).
[4] K. J. Beernink, P. K. York, and J. J. Coleman, Appl. Phys. Lett. **55**, 2585 (1989).
[5] G. M. Smith and J. J. Coleman, in *VLSI Electronics*, edited by N. G. Einspruch and W. R. Frensley (Academic, San Diego, 1994), Vol. 24, pp. 215–238.
[6] G. M. Yang, M. H. MacDougal, and P. D. Dapkus, Electron. Lett. **31**, 886 (1995).
[7] A. Larsson and J. Maserjian, Appl. Phys. Lett. **59**, 3099 (1991).
[8] D. S. McCallum, A. N. Cartwright, X. R. Huang, T. F. Boggess, A. L. Smirl, and T. C. Hasenberg, J. Appl. Phys. **73**, 3860 (1993).
[9] A. Madhukar, K. C. Rajkumar, L. Chen, S. Guha, K. Kaviani, and R. Kapre, Appl. Phys. Lett. **57**, 2007 (1990).
[10] D. H. Rich, H. T. Lin, and A. Larsson, J. Appl. Phys. **77**, 6557 (1995).
[11] D. H. Rich, T. George, W. T. Pike, J. Maserjian, F. J. Grunthaner, and A. Larsson, J. Appl. Phys. **72**, 5834 (1992).
[12] D. H. Rich, K. Rammohan, Y. Tang, H. T. Lin, J. Maserjian, F. J. Grunthaner, A. Larsson, and S. I. Borenstain, Appl. Phys. Lett. **64**, 730 (1994).
[13] E. A. Fitzgerald, G. P. Watson, R. E. Proano, D. G. Ast, P. D. Kirchner, G. D. Pettit, and J. M. Woodall, J. Appl. Phys. **65**, 2220 (1989).
[14] K. Rammohan, Y. Tang, D. H. Rich, R. S. Goldman, H. H. Wieder, and K. L. Kavanagh, Phys. Rev. B **51**, 5033 (1995).
[15] K. Rammohan, D. H. Rich, R. S. Goldman, and K. L. Kavanagh, Appl. Phys. Lett. **66**, 871 (1995).
[16] D. H. Rich, K. Rammohan, Y. Tang, H. T. Lin, R. S. Goldman, H. H. Wieder, and K. L. Kavanagh, J. Vac. Sci. Technol. B **13**, 1766 (1995).
[17] D. Bimberg, J. Christen, A. Steckenborn, G. Weimann, and W. Schlapp, J. Lumin. **30**, 562 (1985).
[18] K. Uno, K. Hirano, S. Noda, and A. Sakaki, in *Proceedings of the 19th International Symposium on GaAs and Related Compounds* (IOP, Bristol, 1993), p. 241.
[19] D. S. Jiang, H. Jung, and K. Ploog, J. Appl. Phys. **64**, 1371 (1988).
[20] U. Jahn, J. Menninger, R. Hey, and H. T. Grahn, Appl. Phys. Lett. **64**, 2382 (1994).
[21] M. Meshkinpour, M. S. Goorsky, G. Chu, D. C. Streit, T. R. Block, and M. Wojtowicz, Appl. Phys. Lett. **66**, 748 (1995).
[22] M. Meshkinpour, M. S. Goorsky, D. C. Streit, T. R. Block, M. Wojtowicz, K. Rammohan, and D. H. Rich, Mater. Res. Soc. Symp. Proc. **340**, 327 (1994).
[23] D. C. Streit, K. L. Tan, R. M. Dia, J. K. Liu, A. C. Han, and J. R. Velebir, IEEE Electron Device Lett. **EDL-9**, 621 (1988).
[24] M. Meshkinpour, M. S. Goorsky, D. C. Streit, T. R. Block, and M. Wojtowicz, Mater. Res. Soc. Symp. Proc. **378**, 783 (1995).
[25] D. H. Rich, A. Ksendzov, R. W. Terhune, F. J. Grunthaner, B. A. Wilson, H. Shen, M. Dutta, S. M. Vernon, and T. M. Dixon, Phys. Rev. B **43**, 6836 (1991).
[26] M. Grundmann, J. Christen, D. Bimberg, A. Hashimoto, T. Fukunaga, and N. Watanabe, Appl. Phys. Lett. **58**, 2090 (1991).

[27]T. E. Everhart and P. H. Hoff, J. Appl. Phys. **42**, 5837 (1971).
[28]H. A. Zarem, P. C. Sercel, J. A. Lebens, L. E. Eng, A. Yariv, and K. J. Vahala, Appl. Phys. Lett. **55**, 1647 (1989).
[29]K. L. Kavanagh, M. A. Capano, L. W. Hobbs, J. C. Barbour, P. M. J. Maree, W. Schaff, J. W. Mayer, D. Pettit, J. M. Woodall, J. A. Stroscio, and R. M. Feenstra, J. Appl. Phys. **64**, 4843 (1988).
[30]T. George, E. R. Weber, S. Nozaki, T. Yamada, M. Konagai, and K. Takahashi, Appl. Phys. Lett. **59**, 60 (1991).
[31]I. Yonenaga and K. Sumino, J. Appl. Phys. **65**, 85 (1989).
[32]R. S. Goldman, H. H. Wieder, and K. L. Kavanagh, Appl. Phys. Lett. **67**, 344 (1995).
[33]D. C. Hutchings, Appl. Phys. Lett. **55**, 1082 (1989).
[34]D. Campi and C. Alibert, Appl. Phys. Lett. **55**, 454 (1989).
[35]S. I. Borenstain, I. Grave, A. Larsson, D. H. Rich, B. Jonsson, I. Andersson, J. Westin, and T. Andersson, Phys. Rev. B **43**, 9320 (1991).
[36]G. Ji, D. Huang, U. K. Reddy, H. Unlu, T. S. Henderson, and H. Morkoç, J. Vac. Sci. Technol. B **5**, 1346 (1987).
[37]F. H. Pollak, in *Semiconductors and Semimetals*, edited by R. K. Willardson and A. C. Beer (Wiley, New York, 1990), Vol. 32, pp. 17–53.
[38]S. L. Chuang, Phys. Rev. B **43**, 9649 (1991).
[39]S. Adachi, J. Appl. Phys. **53**, 8775 (1982).
[40]J. D. Lambkin, L. Considine, S. Walsh, G. M. O'Connor, C. J. McDonagh, and T. J. Glynn, Appl. Phys. Lett. **65**, 73 (1994).
[41]B. G. Yacobi and D. B. Holt, J. Appl. Phys. **59**, R1 (1986).
[42]J. I. Pankove, *Optical Processes in Semiconductors* (Dover, New York, 1971), p. 166.
[43]See, for example, N. W. Ashhcroft and N. D. Mermin, *Solid State Physics* (Saunders College, Philadelphia, 1976), pp. 602–605.